Supplementary Information

Servann Herou[†], Maria Crespo Ribadeneyra[†], Rajesh Madhu[†], Vicente Araullo-Peters[†], Anders Jensen[†], Philipp Schlee[†] and Magdalena Titirici[†]

Affiliations

[†] Queen Mary University of London, School of Engineering and Materials Science, Materials Research Institute, Mile End Road, E1 4NS, London, UK

1. Methods

Lignin characterization. **Gel permeation chromatography (GPC)** measurements were conducted on an Agilent 1260 infinity system operating in DMF with 5mM NH_4BF_4 and equipped with refractive index detector and variable wavelength detector, two PLgel 5 µm mixed-C columns (300 × 7.5 mm), a PLgel 5 mm guard column (50 × 7.5 mm) and an autosampler. The instrument was calibrated with linear narrow poly-styrene (PS) standard. The organosolv lignin was dissolved in DMF at a concentration of 1mg/mL of solvent, sonicated and filtered through 0.2 µm Nylon filters before analysis. **Two-Dimensional Heteronuclear Single Quantum Coherence (2D-HSQC) (^{1}H &^{13}C) Nuclear magnetic resonance (NMR)** spectra were recorded on a Bruker AV-III 600 MHz. The organosolv lignin was dissolved in dimethyl sulfoxide-d6, 99.9 atom % D [$(CD_3)_2SO$] at a concentration of 30mg/mL and the resonance signal of residual $(CD_3)_2SO$ at 2.5 ppm (^{1}H) and 40 ppm (^{13}C) served as reference for the chemical shift δ. **^{31}P NMR spectroscopy** was used to quantify the hydroxyl groups after derivatization of lignin with 100 µL of 2-chloro-4,4,5,5-tetramethyl-1,3,2-dioxaphospholane (TMDP).[1,2,3] The lignin sample (30 mg) was dissolved in dimethylformamide/pyridine (1:1 v/v) and mixed with 100 µL of a solution of N-hydroxy-5-norbornene-2,3-dicarboxylic acid imide (20 mg/mL) and chromium(III) acetylacetonate (5 mg/mL) as internal standard and relaxation agent, respectively. ^{31}P NMR spectra were acquired using an inverse-gated decoupling pulse sequence with a 90 ° pulse angle, 10 s relaxation delay, and 512 scans.

2. Characterisation

2.1 Organosolv lignin characterisation

2.1.1. *2-Dimensional (^{13}C-^{1}H) Heteronuclear Single Quantum Coherence*

The structural features of organosolv lignin were determined by **HSQC-2D (^{13}C-^{1}H) NMR**. This technique has recently shed light on lignin structures and has been used to analyse the interunit bonding units of various lignins extracted from biomass [4,5,6,7,8]. It also gives an indication on the amount of non-hydrolysed carbohydrates remaining linked on the lignin branches.

The beech extracted organosolv lignin consists of mono-units and interlinkages typically observed in hardwood lignins, as shown in Figure S1. Clear hydrocarbon peaks

could not be observed even at lower contours levels assessing that the carbohydrate content of the organosolv lignin stays below detection level. The side-chain region of the 2D HSQC NMR spectra (left) (δC/δH 20-100/2.0-5.4) shows the high concentration of methoxyl groups (region1) observed at δC/δH 53.65-57.04/3.53-3.88 [4,8]. The second most recognizable group in region 2 (δC/δH 59.5-61.25/3.38-3.75) corresponds to the A_γ carbon atom (see Figure S2)[4,7]. This shows the presence of numerous hydroxyl groups -OH in comparison to ketone -C=O groups. The regions 3 (δC/δH 4.17-4.2 / 71.2-72.12) and 4 (δC/δH 4.6-4.68/85.2-86.13) respectively correspond to the B_γ and B_α carbon in the B unit indicating the presence of β-β' linkages in the organosolv lignin. In native hardwood lignins, approx. 3% of linkages are β-β' linkages. The region 5 (δC/δH 4.55/80.65) corresponding to the A_β carbon on is very weak but appears at lower contours level especially on the 1H spectrum. This low concentration of β-O-4 linkages in the organosolv lignin has also been shown by Zakzeski et al.[7]. The clear peaks at δC/δH 30-47/2.1-3.0 corresponds to DMSO and the proton peak at δH 3.4 to water since DMSO tends to trap water.

The aromatic region of the 2D HSQC NMR spectra (right) (δC/δH 70-150/5-9) shows a high concentration of syringyl units. The regions 6 (δC/δH 103.6-108.1/6.275-6.85) and 7 (δC/δH 107-107.5/7.23) corresponds respectively to the S_2 & S_6 carbon atoms as well as S'_2 & S'_6 carbon atoms[4,9]. At higher contours level we can observe the presence of guaicyl groups in much smaller concentration in region 8 (δC/δH 115-117/6.58-6.77), 9 (δC/δH 123.5/7.54-7.58), and 10 (δC/δH 110-113/7.16) respectively corresponding to the G_2 & G_6 carbon atoms, G'_6 and G'_2.

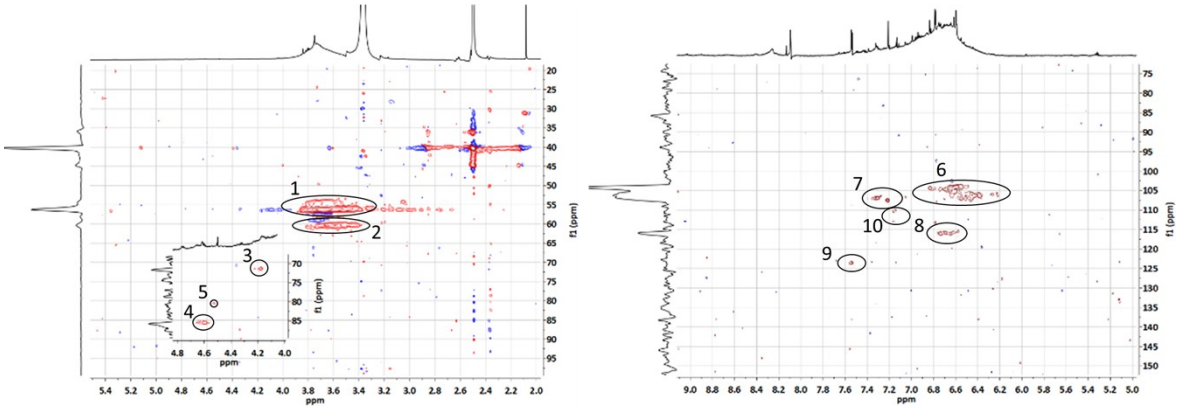

Figure S1: Side-chain (left) and aromatic regions (right) in the 2D HSQC NMR spectra: δC/δH 25-100/2.0-5.6 and δC/δH 75-150/5.0-9.0 of OSL extracted from beech wood by organosolv method.

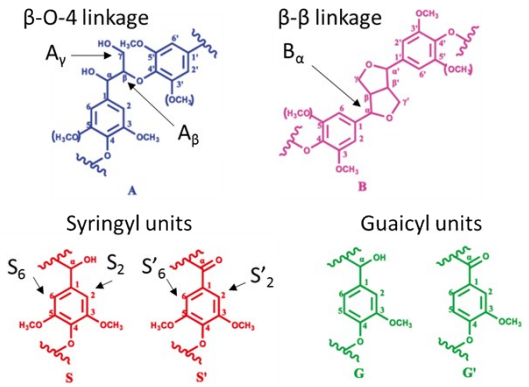

Figure S2: Annotations of the lignin structure present in the organosolv beech lignin. Taken from ref [4]

2.1.2. *Gel permeation Chromatography and hydroxyl groups quantification via ^{31}P-NMR*

The molecular weight of the OSL was estimated by **Gel Permeation Chromatography** and calculated versus polystyrene (PS) as recommended by Lange, Tolbert et al.[10,11] The OSL is highly dispersed with a molecular weight of M_w/M_n/PID of 4815g.mol^{-1}/3207g.mol^{-1}/1.50 versus PS (see Figure S3b). The polydispersity is quite low compared to the literature but the molecular weight is comparable [12,13].

^{31}P-NMR was used to quantify the various hydroxyl groups contained in the organosolv lignin. As indicated by 2D-HSQC NMR, we can observe a higher quantity of syringyl -OH than guaicyl -OH groups (1.4 *vs* 0.6 mmol.g^{-1}), characteristic of hardwood lignins. The low carboxylic acid content indicate a low oxidation degree for this lignin.

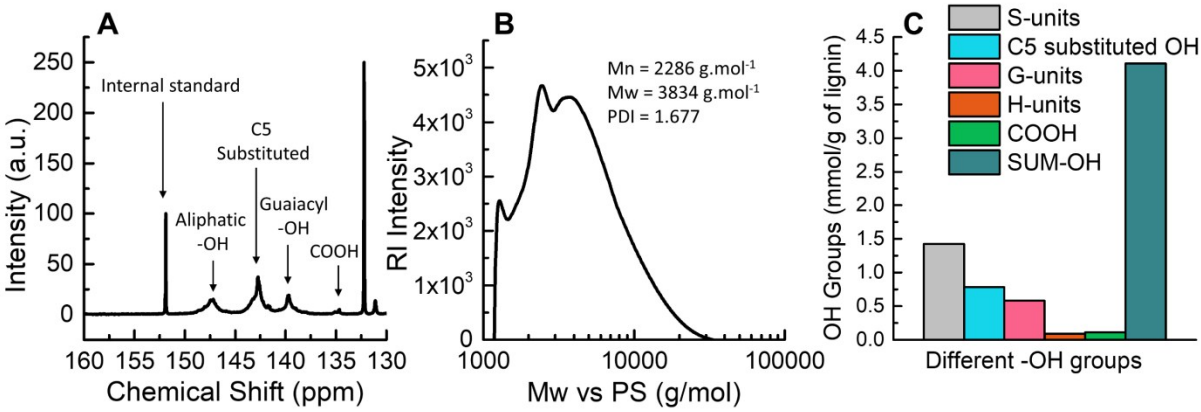

Figure S3: a) ^{31}P-NMR spectrum; b) GPC molecular weight distribution and c) Hydroxyl groups present in the organosolv lignin as determined by the ^{31}P-NMR analysis.

2.2 SAXS characterisation

The fit where made with the following function[14]:

$$I(Q) = \frac{A}{Q^4} + \frac{Ba_1^4}{\left(1 + a_1^2Q^2\right)^2} + \frac{C}{1 + a_2^2Q^2} + I_{bg} \qquad \textit{(eq S1)}$$

2.3 Electrode density measurements

The electrode density was calculated from the following equation:

$$\rho_{electrode} = \frac{1}{V_{totDFT} - \frac{1}{\rho_{bulk}}} \quad \textit{(eq S2)}$$

The value of ρ_{bulk} was estimated of 2.1 g.cm^{-3} but could vary between 2.0 and 2.2 g.cm^{-3} and the corresponding error was reported in Table 1.

Differences in pore structure between PG, PLG and LG translates in different electrode densities of 0.7 g.cm^{-3}, 0.9 g.cm^{-3} and 1.1 g.cm^{-3}, respectively (see Table S1 for details on the porosity). This density increases upon incorporation of lignin in the system impacts the volumetric performance and an optimum can be found which combines both sufficiently high porosity and high density.

2.4 Electrochemical characterisation

The capacitance dependant on the cell potential was calculated from the cyclo-voltammograms (*eq S3*), the capacitance retention was calculated from the cyclo-voltammograms (eq S4) and the galvanostatic charge discharge (*eq S5)* and the impedance spectroscopy (*eq S6*) as following:

$$C_{CV} = \frac{4.I}{\nu.X} \quad \textit{(eq S3);} \qquad C_{CV} = \frac{4.Q}{\Delta V.X} \quad \textit{(eq S4)}$$

$$C_{GCD} = \frac{4.Q}{(\Delta V - IR_{drop}).X} \quad \textit{(eq S5)} ; \qquad C_{EIS} = \frac{4.\left|Z^{''}(\omega)\right|}{2\pi\omega\left(Z^{'}(\omega)^2 + Z^{''}(\omega)^2\right).X} \quad \textit{(eq S6)}$$

The following notations are used: I(mA) current, ν(mV/s) scan rate of the cyclo-voltammograms, Q(C) the charge accumulated in the porous material calculated during the discharge cycle, ΔV(V) is the voltage window, IR_{drop} (V) is the voltage drop observed when the current is reverse during GCD, ω(Hz) is the frequency, Z'(Ω) and Z"(Ω) the real and imaginary parts of the impedance and X the specific parameter. X is the mass of the working electrode in grams in case of gravimetric capacitance, surface of the working electrode in cm^2 in case of areal capacitance and volume of working electrode in cm^3 in case of volumetric capacitance.

The Ragone plot is built from the galvanostatic charge discharge curves by dividing the discharged energy of the cell (for each current density tested) by the total volume of the electrodes (sum of the two electrodes).

The cell resistance $R(\Omega)$ was calculated by measuring the $IR_{drop}$for each current density measured above 10 A/g (the IR_{drop} is more visible at high current densities) and determining the slope R of the following curve

$$IR_{drop}(V) = R(\Omega).i(A) \quad \textit{(eq S7)}$$

3. Results and discussion

3.1 Solubility of the organosolv lignin

The organosolv lignin used herein has a higher solubility in acetone than in ethanol although the Hansen solubility parameters for lignin mono-units are reported to be closer to ethanol (δ_{lignin}≈13-14; $\delta_{acetone}$=9.8; $\delta_{ethanol}$=12.1)[15]. We believe that this is due to the steric effect of lignin entanglement which makes acetone more suitable to dissolve lignin due to its aprotic nature (fig. S4). Hence we chose acetone as the solvent choice for this study.

Figure S4: Pictures of the beech extracted organosolv lignin solubilised in acetone (left) and ethanol (right) at a concentration of 100mg/mL. The lignin was grounded prior to solubilisation and the two solutions were sonicated for 20min. We can observe a better solubility of lignin in acetone than in ethanol.

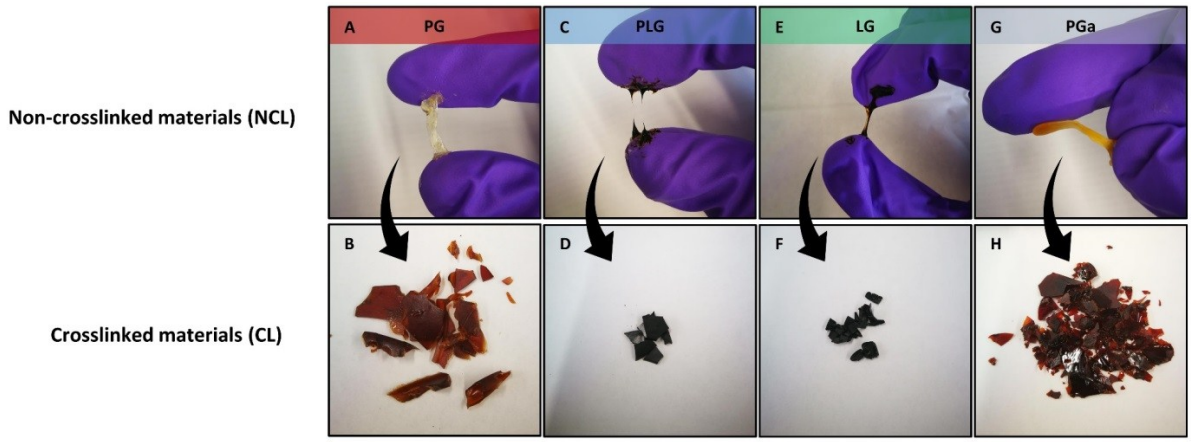

Figure S5: Pictures of the samples before and after crosslinking. a,b) PG; c,d) PLG; e,f) LG and g,h) PGa. After crosslinking, PG and PGa show very brittle structure whereas PLG and LG which contain lignin are more rubbery.

3.2 Textural properties of the carbonised materials

Table S1: Porosity data for PG (0wt% lignin), PLG (50wt% lignin) and LG (100 wt% lignin) calculated from N_2 adsorption isotherms (DR, DFT and BJH models) or from SAXS (Porod's model).

	S_{BET} ($m^2.g^{-1}$)	S_{DR} ($m^2.g^{-1}$)	V_{DR} ($cm^3.g^{-1}$)	S_{DFT} ($m^2.g^{-1}$)	$V_{TOT\ DFT}$ ($cm^3.g^{-1}$)	$\frac{V_{MICRO}}{V_{TOTAL}}$ (%)	S_{BJH} ($m^2.g^{-1}$)	V_{BJH} ($cm^3.g^{-1}$)	Mean pore diameter D_0 (nm)	d_{100} from SAXS	Lattice parameter a_0 (nm)	Wall thickness t_w (nm)
PG	763	753	0.268	783	0.81	17%	411	0.66	7.3	12.1	13.97	7.02
PLG	667	673	0.239	678	0.51	27%	300	0.34	3.9	9.7	11.20	7.48
LG	81	92	0.033	76	0.11	15%	31	0.084	3.621	NA	NA	NA

The mean pore diameter was calculated by the BJH model and the wall thickness was calculated using the following equation reported by ref [16]:

$$t_w = \frac{2}{\sqrt{3}} * d_{100} - \frac{D_0}{1.050} \quad \textit{(eq S8)}$$

3.3 Difference of morphology between glyoxal (PG) and glyoxylic acid (PGa) systems

3.3.1. Characterisation of the crosslinking

Thermogravimetric analysis (TGA) shows for PG an enhanced thermal stability when compared to PGa, showing the higher number of cross-links created by the glyoxal compared to the glyoxylic acid.

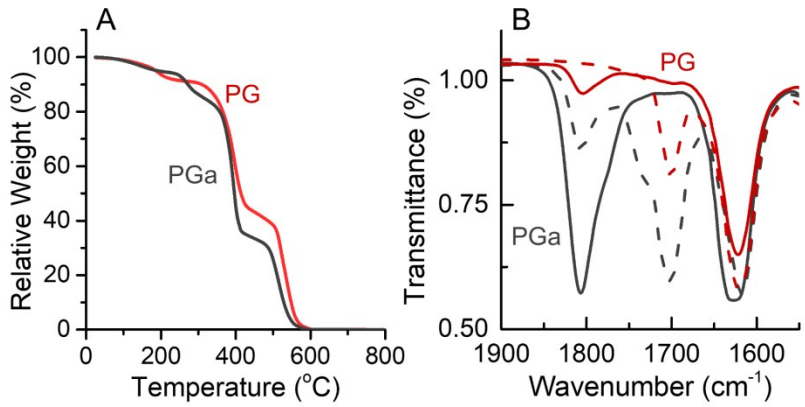

Figure S6: a) Thermogravimetric analysis under air at 10°C/min of the samples after crosslinking; b) FTIR spectrums of the crosslinked (solid lines) and non-crosslinked (dashed lines).

FTIR was also used to analyse the different crosslinking between the sample PGa and PG. We observe for both PG and PGa samples a peak at 1610 cm^{-1} corresponding to the stretching vibration of C=C in phloroglucinol, glyoxal and glyoxylic acid. The wide peak of glyoxylic acid is visible on the composite material PGa. The peaks at 1700-1732cm^{-1} (C=O in COOH and aldehyde respectively) present in PGA before crosslinking disappears upon thermal treatment to form a peak at 1805 cm^{-1} assimilated to cyclic lactones[17]. In the case of PG, the peak at 1700 cm^{-1} is still present after crosslinking, indicating that not all the glyoxal reacted.

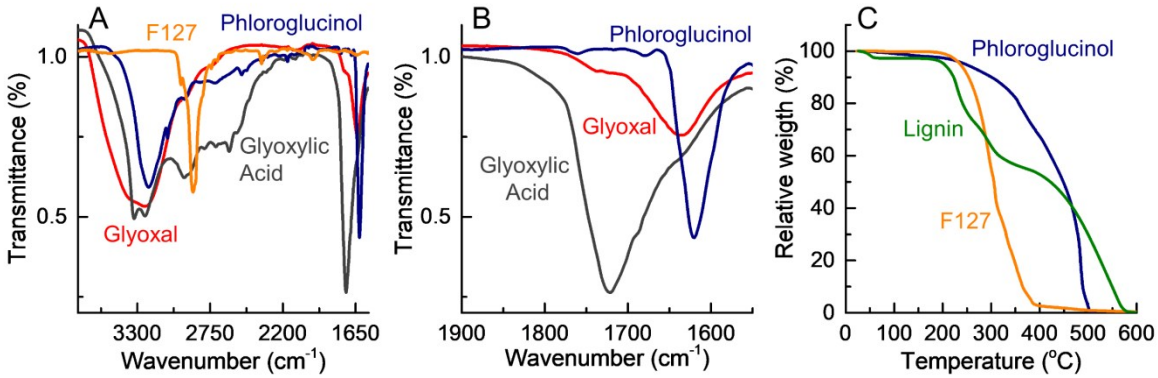

Figure S7: a) FTIR spectrums of the raw compounds; b) Zoom on the FTIR spectrum; c) Thermogravimetric analysis under air at 10°C/min of the raw compounds

3.3.2. Physico-chemical of the carbonised materials

After carbonisation, we observe that the soft templated materials exhibit different porous architectures. TEM micrographs (Figure S8a-8d) reveal for C-PG a well-ordered 2D hexagonal structure (*p6m*) with an interpore distance of approximately 12nm in the plane (100) and a pore size varying between 5 and 8nm. On the other hand, C-PGa shows a hardly

ordered structure with interrupted cylindrical pores indicating that without the presence of catalyst, glyoxylic acid does not effectively crosslink the phloroglucinol to retain the mesoporous network upon carbonisation.

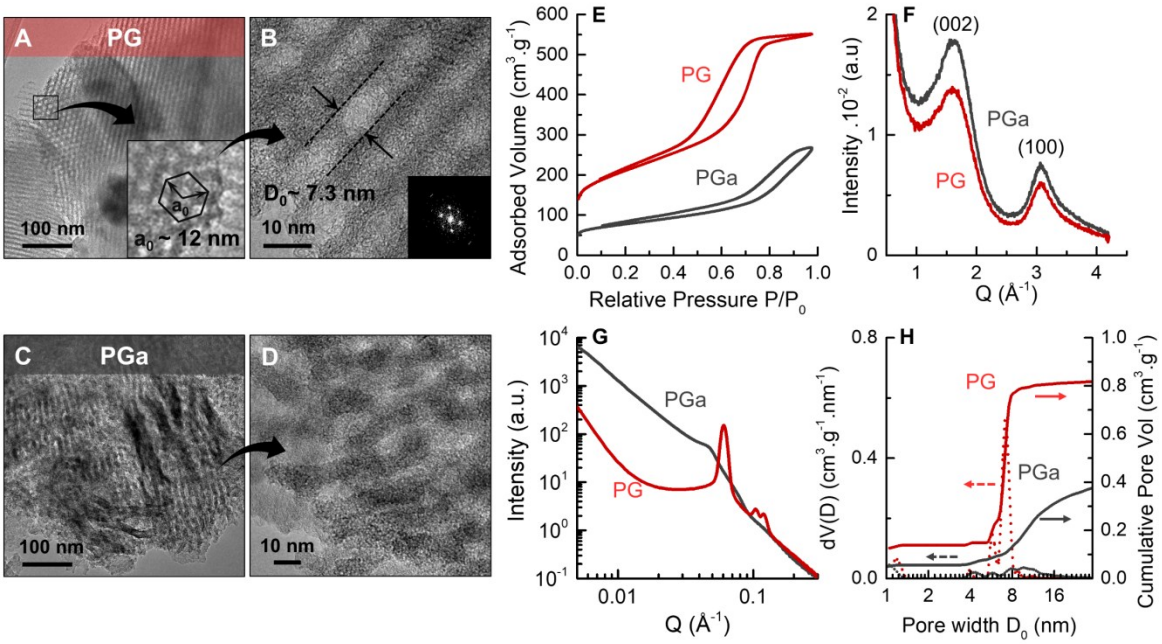

Figure S8: a,b) TEM micrographs of the carbonised PG sample; c,d) TEM micrographs of the carbonised PGa sample. The insets showed on a) the detailed hexagonal structure and on b) FFT on micrograph on picture 1a; e) N2 adsorption isotherms measured at 77K; f) WAXS and g) SAXS diffractograms of both samples; h) Pore size distribution calculated from QSDFT model on the adsorption line;

The N_2 isotherms and the pore size distribution (Figure S8e and S8h) reveal that both samples are mostly mesoporous. The glyoxal sample (PG) exhibits a pore volume of 0.8 $cm^3.g^{-1}$, which is double than its glyoxylic acid counterpart (PGa). In the latter, the interruption of the porous network is accompanied with a wide range of pore sizes from 4 to 20nm whereas PG shows defined pore sizes of 7nm. The hysteresis observed on both N_2 ad-desorption isotherms (Figure S8e) also reveal differences in the pore shapes. The long and thin hysteresis observed for PGa indicates the presence of pores which are more opened than the bottleneck pores of PG (Figure S9).

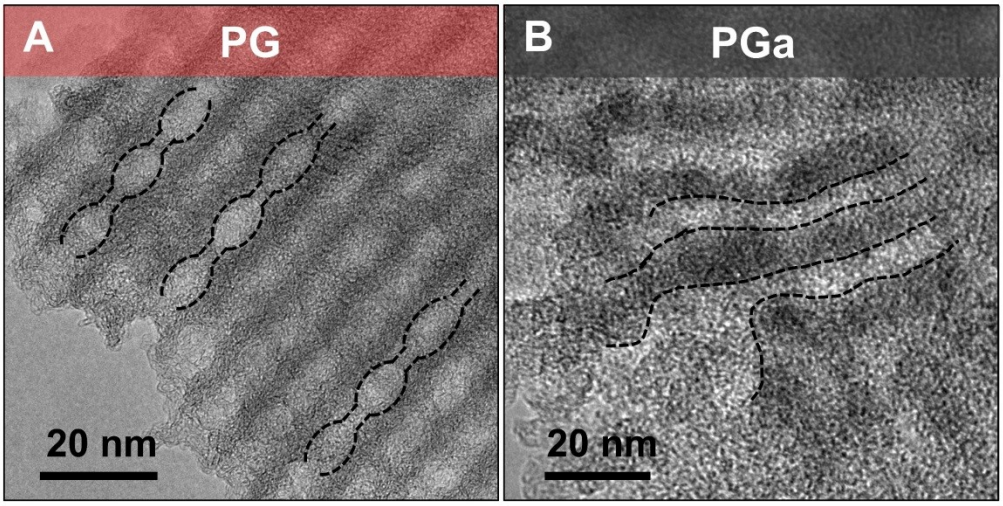

Figure S9: TEM micrographs showing the interconnected porous network of a) PG and b) PGa. The pores in PG can be considered as interconnected series of spherical pores whereas PGa exhibits opened pores.

SAXS diffractograms confirms a significant difference between the two samples (Figure S8g). C-PGa shows a broad shoulder at 0.04 $Å^{-1}$ but with no clear periodic structure. On the other hand, C-PG shows a main peak at 0.06 and two smaller ones at 0.10 and 0.12 $Å^{-1}$ corresponding to the (100), (110) and (200) peaks of a 2D hexagonally ordered porous structure (similar to the MCM-41, SBA-15 or even KIT-6)[18]. The pore to pore distance, corresponding to the d_{001} interplanar spacing, was calculated at 12.1nm, which consistent with the TEM observations. An additional Porod's fit suggests nanopores with a radius of 2.9nm (eq. S1). These smaller pores are common in hard carbons and are likely to reside in the wall structure between the ordered pores. The combination of the BJH calculation with the interplanar spacing of the porous network enables an estimation of the wall thickness around 7.02nm for C-PG. The high Q region (>1 $Å^{-1}$) of the diffractogram (Figure S8f) shows the characteristic peaks of hard carbon, with the (002) peak at ~1.8 $Å^{-1}$ related to the distance between graphitic layers and the (100) peak at 3 $Å^{-1}$ related to the C=C distances in the plane of the graphitic layers. As seen by the similarity of these peaks the different crosslinker both result in similar atomic structure. The peak position and line broadening suggests that the hard carbon samples as a layer spacing of 3.805 Å with an average of 2-3 layers in a stack. The (100) peak showed in a plane distance of 2.0515 Å slightly smaller than the corresponding distance in graphite of 2.13 Å, suggesting the presence of defects in the graphitic layers.[19]

3.4 Electrochemical characterisation of the C-PG, C-PLG and C-LG

LG is not considered as a super-capacitive material and its volumetric performances are very low, in accordance with its morphology. The shape of the cyclo-voltammogram (CV) (Figure S10e,f) and the charge discharge curve (GCD) at low current density suggests first a poor capacitive behaviour due to the non-rectangular shape of the CV as well as the presence of a reversible faradaic contribution at high overpotential. This behaviour is typically observed when the carbon surface is being oxidised and reversibly reduced (>90% coulombic efficiency measured) at high overpotentials. The impedance (EIS) measurement

confirms that LG does not show any capacitive region over the frequency range 10mHz-200kHz, characterised by a phase angle of -90° (Figure S10c).

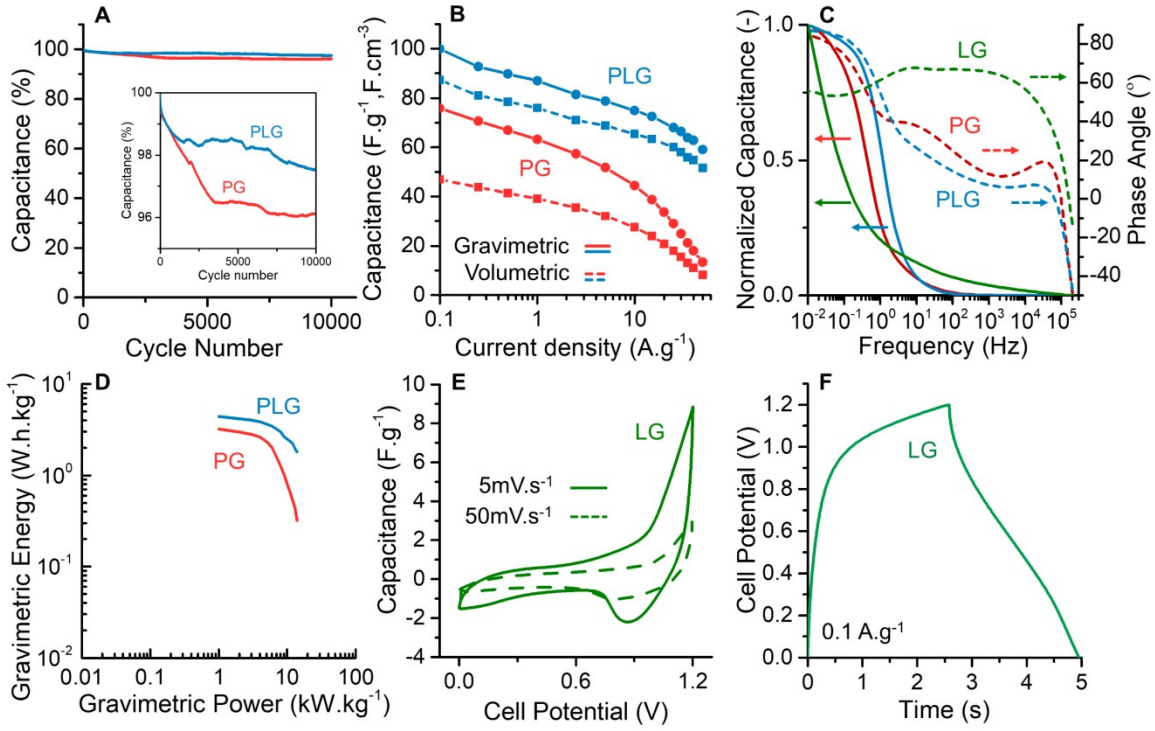

Figure S10: a) Cyclability on the samples PLG and PG at 10 A.g^{-1} in the two-electrodes Swagelok cell; b) Galvanostatic Charge Discharge curves of the samples PLG and PG in the two-electrodes Swagelok cell; c) Electrochemical Impedance Spectroscopy measurements on PG, PLG and LG showing the phase angle (dashed lines) and the real capacitance decay with increasing frequency; d) Gravimetric Ragone plot of PG and PLG; e) Cyclo-voltammogram of sample LG at 5 mV/s (solid line) and 50 mV/s (dashed line); f) Galvanostatic Charge Discharge curve of sample LG at 0.1 A.g^{-1};

3.5 *Ionophilicity and wetting on the soft templated materials*

The ionophilicity of the material with the electrolyte used (6M KOH) was tested via two methods. We first performed X-rays photoelectron spectroscopy (XPS) analysis on the materials to obtain information on the surface oxygen groups, known to provide better ionophilicity with polar electrolytes. Then we performed a series of wetting cycles at 5 A.g^{-1} to ensure that the electrochemical performances tested were obtained in proper conditions (stable and with the maximum pore penetrability). The wetting cycles are presented in Figure S11 and the XPS results in table S2 and Figure S12.

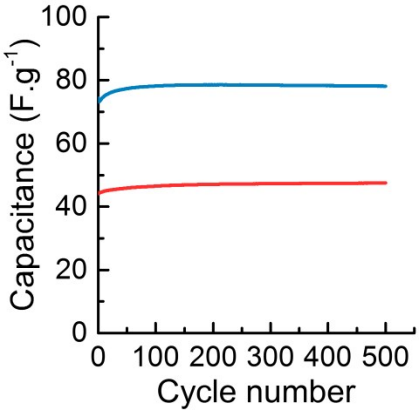

Figure S11: Wetting cycles performed prior to electrochemical analysis. The increase in capacitance observed is explained by a better wettability of the material, characterised by a better contact between the electrolyte and the porous surface.

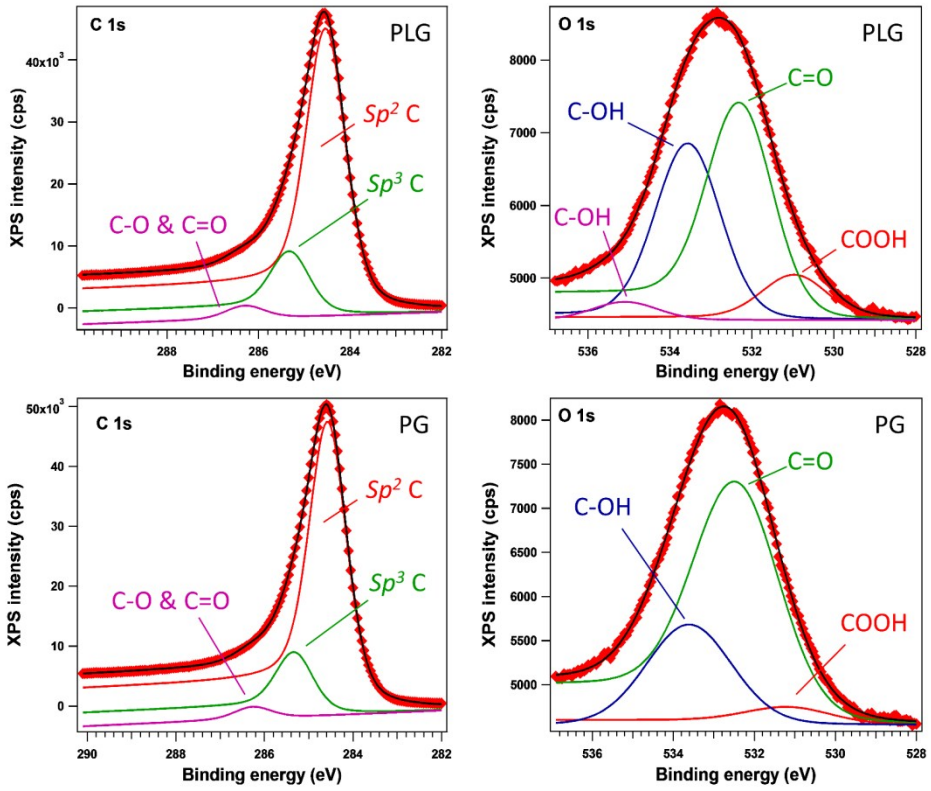

Figure S12: X-Rays photoelectron spectroscopy of PG and PLG showing the different carbon and oxygen bonds as well as the associated energies.

Table S2: X-Rays Photoelectron spectroscopy on PLG and PG after carbonisation

PLG			PG		
C 1s	**O 1s**	**N 1s**	**C 1s**	**O 1s**	**N 1s**
284.5	531.0	399.8	284.6	531.1	399.6
285.3	532.3	-	285.3	532.4	-
286.3	533.6	-	286.3	533.6	-
-	535.1	-	-	534.6	-
Total	**Total**	**Total**	**Total**	**Total**	**Total**

93.40%	6.46%	0.08%	94.40%	5.31%	0.26%

References

1 A. Granata and D. S. Argyropoulos, *J. Agric. Food Chem.*, 1995, **43**, 1538–1544.

2 J. Rönnols, H. Schweinebarth, A. Jacobs, J. S. Stevanic, A. Olsson and A. Reimann, *Nord. Pulp Pap. Res. J.*, 2015, **30**, 550–561.

3 Y. Pu, S. Cao and A. J. Ragauskas, *Energy Environ. Sci.*, 2011, **4**, 3154–3166.

4 T. Q. Yuan, S. N. Sun, F. Xu and R. C. Sun, *J. Agric. Food Chem.*, 2011, **59**, 10604–10614.

5 R. Samuel, Y. Pu, B. Raman and A. J. Ragauskas, *Appl. Biochem. Biotechnol.*, 2010, **162**, 62–74.

6 M. Sette, H. Lange and C. Crestini, *Comput. Struct. Biotechnol. J.*, 2013, **6**, e201303016.

7 J. Zakzeski, A. L. Jongerius, P. C. A. Bruijnincx and B. M. Weckhuysen, *ChemSusChem*, 2012, **5**, 1602–1609.

8 M. Hedenström, S. Wiklund-Lindström, T. Öman, F. Lu, L. Gerber, P. Schatz, B. Sundberg and J. Ralph, *Mol. Plant*, 2009, **2**, 933–942.

9 S. Yang, J.-L. Wen, T.-Q. Yuan and R.-C. Sun, *RSC Adv.*, 2014, **4**, 57996–58004.

10 H. Lange, F. Rulli and C. Crestini, *ACS Sustain. Chem. Eng.*, 2016, **4**, 5167–5180.

11 J. R. Allison Tolbert, Hannah Akinosho, Ratayakorn Khunsupat, Amit K. Naskar, *Biofuels, Bioprod. Biorefining*, , DOI:10.1002/bbb.1500.

12 A. Abaecherli, M. Fasching, B. Hortling, J. Li, E. De Jong, U. M. R. Chimie and B. Agroparistech, *Holzforschung*, 2007, **61**, 459–468.

13 C. G. Yoo, M. Li, X. Meng, Y. Pu and A. J. Ragauskas, *Green Chem.*, 2017, **19**, 2006–2016.

14 D. A. Stevens and J. R. Dahn, *J. Electrochem. Soc.*, 2000, **147**, 4428.

15 and G. H. Nicola Giummarella, Christofer Lindgren, Mikael E. Lindström, *Bioressources*, 2016, **11**, 3494–3510.

16 M. Kruk, M. Jaroniec, Y. Sakamoto, O. Terasaki, R. Ryoo and C. H. Ko, *J. Phys. Chem. B*, 2000, **104**, 292–301.

17 C. Matei Ghimbeu, L. Vidal, L. Delmotte, J.-M. Le Meins and C. Vix-Guterl, *Green Chem.*, 2014, **16**, 3079.

18 P. Selvam, S. K. Bhatia and C. G. Sonwane, *Ind. Eng. Chem. Res.*, 2001, **40**, 3237–3261.

19 R. W. G. WYCKOFF., *Crystal structures. Vol. I.*, New York, London, Sydney, Interseien., 1963.

***